

**Densities and speeds  
in an arc-heated supersonic  
argon beam**

E.L. KNUTH, N.M. KULUVA  
and J.P. CALLINAN

FACILITY FORM 602

N 71-72245	(THRU)
(ACCESSION-NUMBER)	None
10	(CODE)
(PAGES)	
CR-117447	(CATEGORY)
(NASA CR OR TMX OR AD NUMBER)	



Article paru dans Entropie n° 18 de novembre-décembre 1967.

Sgt- 64618

# Densities and speeds in an arc-heated supersonic argon beam <sup>(1)</sup>

E. L. KNUTH, N. M. KULUVA <sup>(2)</sup>  
and J. P. CALLINAN <sup>(3)</sup>

Department of Engineering  
University of California, Los Angeles (U.S.A.)

Argon molecular beams at intermediate energies and high intensities are obtained by heating the beam gas in an electric arc and by converting the thermal motion into energy of directed motion in a supersonic free-jet.  $\curvearrowright$  The performance of this facility has been measured and compared with the predicted characteristics of a model of molecular beams using a free supersonic jet.  $\curvearrowright$  An energy of 2,7 eV was reached. It is hoped to reach higher energies by using a constricted arc.

Des jets moléculaires d'argon à des énergies moyennes et de fortes intensités sont obtenus en chauffant le jet gazeux dans un arc électrique et en transformant l'énergie thermique en une énergie dirigée suivant un écoulement libre supersonique.  $\curvearrowright$  Les résultats obtenus par ce dispositif ont été comparés avec les caractéristiques que l'on peut prévoir à partir d'un modèle de production de jets moléculaires utilisant un écoulement supersonique libre.  $\curvearrowright$  On a pu atteindre une énergie de 2,7 eV. On espère en utilisant un arc étroit obtenir des énergies plus grandes.

Argon-Molekularstrahlen mittlerer Energie und hoher Intensität werden erzeugt indem man einem Gasstrahl elektrisch erhitzt und dabei die thermische Energie in eine gelenkte Energie nach einem überschallfluss, umwandelt.  $\curvearrowright$  Die mit dieser Vorrichtung erzielte Ergebnisse wurden mit den Eigenschaften verglichen, die man, an Hand eines Molekularstrahle erzeugungsmodell das den freien Überschallfluss anwendet, voraussehen kann.  $\curvearrowright$  Man konnte Energien bis zu 2,7 eV erreichen und man hofft noch höhere Energien zu erreichen.

Chorros moleculares de argón con energías medias y fuertes intensidades se obtienen calentando el chorro gaseoso en un arco eléctrico y transformando la energía térmica en una energía dirigida que siga un flujo libre supersónico.  $\curvearrowright$  Los resultados obtenidos por este dispositivo se han comparado con las características que pueden preverse a partir de un model de producción de chorros moleculares en la que se utilice un flujo supersónico libre.  $\curvearrowright$  Ha sido posible alcanzar una energía de 2,7 eV. Se espera que, utilizando un arco estrecho, han de poder obtenerse energías mayores.

## 1 INTRODUCTION

The speed and intensity limitations of conventional oven and ion beams have motivated, during the past decade, several programs for developing molecular beams with energies from 1 to 10 electron-volts (useful, e.g., in studies of chemical reactions and molecule-satellite collisions) and/or for increasing the intensity of the molecular beam (in order to facilitate detection after filtering and scattering). One finds, as is apparent in the papers presented in this Symposium, that most of these programs use the supersonic molecular beam (a beam which uses a supersonic jet as a source) in order to increase the beam intensity. Methods used for producing beam energies from 1 to 10 eV include accelerating a small mole fraction of a high-molecular-weight gas by a large mole fraction of a low-molecular-weight gas, expanding a gas compressed in a shock tube, and expanding a gas heated in an electric arc.

An arc-heated supersonic molecular beam is used at UCLA to increase the intensity and provide energies above 1 eV. Relative to the binary beam, it has only one gas component whereas, relative to the shock-tube beam, it operates in a steady state. In the

present paper, the review of this facility presented in May 1966 (Ref. [1]) is updated. A brief description of the apparatus is followed by more detailed reviews of the beam density and speed distribution and by brief summaries of other beam properties and applications.

## 2 APPARATUS

New apparatus features since the review of reference [1] include (a) the use of a single-disc chopper (rather than a two-disc chopper-filter) and an orbitron detector (rather than a detector with either a Nier ionizer or a Heil ionizer) in recent beam-density measurements and (b) the recent addition of another 10-inch diffusion pump to the collimating chamber. Nominal descriptions of the apparatus (Fig. 1) for jet

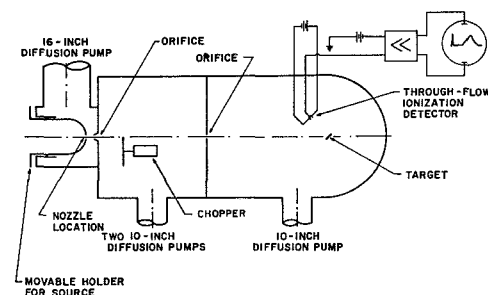


Fig. 1 Schematic Diagram of UCLA Supersonic Molecular Beam

<sup>(1)</sup> Supported chiefly by NSF Grant GK-580, also by NASA Grant NsG-237-62.  
<sup>(2)</sup> Present address: Research Dept., Rocketdyne, Canoga Park, Calif.  
<sup>(3)</sup> Present address: Mechanical Engineering Dept., Loyola Univ., Los Angeles, Calif.

production, beam collimation, speed determination, and beam detection are provided here. Extended descriptions are found in references [1] and [2].

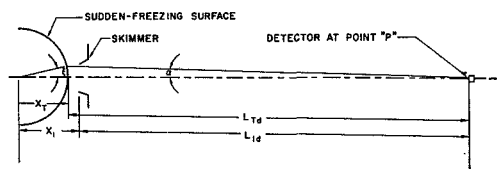


Fig. 2 Geometry of Model Used in Prediction of Beam Density at Detector

The high-speed argon jet is produced by heating the argon in the arc between two tungsten electrodes and then expanding the high-enthalpy argon through a converging nozzle into the partially evacuated source chamber (fig. 3, Ref. [1]). The arc was operated with a potential difference of about 14 volts and at currents up to about 300 A. Effective diameters of the nozzle throat ranged from 0.55 to 1.97 mm. Source-chamber pressures from  $5 \times 10^{-3}$  to  $3 \times 10^{-1}$  Torr were maintained by a 16-inch Stokes booster diffusion pump with a net speed of about 2300 liters/sec for argon when backed by a 140 cfm Stokes mechanical pump. The maximum Mach number obtainable in the free jet was limited either by shock waves (for sufficiently large values of source-chamber pressure divided by stagnation-chamber pressure) or by translational-freezing (for sufficiently large values of translational-relaxation time divided by gas-expansion time). Beam energies greater than obtained in either binary-mixture or arc-heated beams might be obtained in an arc-heated binary-mixture beam.

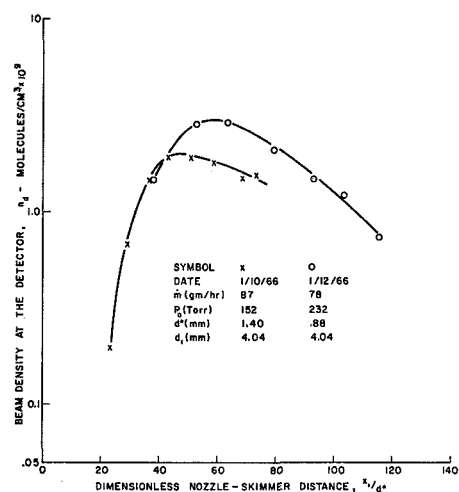


Fig. 3 Beam Density vs. Dimensionless Nozzle-Skimmer Distance

The beam was collimated by a skimmer attached to the wall separating the source and collimating chambers and by an orifice in the wall separating the collimating and detection chambers. The several

skimmers (all conical) included the following combinations of dimensions:

- (a)  $d_1 = 0.051$  cm,  $\delta_i = \delta_e = 30^\circ$ ,
- (b)  $d_1 = 0.114$  cm,  $\delta_i = \delta_e = 30^\circ$ ,
- (c)  $d_1 = 0.152$  cm,  $\delta_i = 28^\circ$ ,  $\delta_e = 37^\circ$ , and
- (d)  $d_1 = 0.404$  cm,  $\delta_i = 15^\circ$ ,  $\delta_e = 25^\circ$

where  $d_1$  is the orifice diameter,  $\delta_i$  is the internal half-apex angle, and  $\delta_e$  is the external half-apex angle. For most of the beam-performance studies, the collimating-orifice diameter was 0.64 cm. The two orifices were separated by about 1 m. In earlier performance measurements, the collimating chamber was pumped only by a 10-inch CVC diffusion pump connected to the chamber by a right-angle valve and backed by a 15 cfm Hereaus mechanical pump. In later measurements, this pumping system was supplemented by a 10-inch CVC diffusion pump connected directly to the chamber and backed by a 15 cfm Welch mechanical pump. The maximum density obtainable in the collimated beam was limited by background scattering in the collimating and source chambers.

The speed distribution in the beam was determined by the time-of-flight technique. The beam was chopped into relatively short bursts by an 17.8-cm diameter disc containing two equally spaced  $1^\circ$  slots and rotated by a synchronous motor (manufactured by the Connecticut Division of the Electronic Specialty Company) at speeds up to 25,000 rpm (fig. 9, Ref. [1]). It was located in the collimating chamber (rather than in the detection chamber) in order (a) to increase the flight path and (b) to decrease the noise in the detector circuit. The two-disc turbine-driven chopper-filter was used (with a reduced phase angle of about  $4^\circ$ ) only in the earlier beam-density measurements.

The beam density was measured using an electron-impact ionization detector of either the Nier-ionizer type (fig. 6, Ref. [1]) the Heil-ionizer type, or the orbitron type (figure 3, Ref. [3]). In all three types, the ions produced by bombardment of the molecules by electrons are attracted to the ion collector and neutralized. The potential drop caused by the flow of neutralizing electrons through a resistor in series with the ion collector is amplified by a Keithley Model 102B decade isolation amplifier, averaged by a Northern Scientific Model NS-513 digital memory oscilloscope, and transferred to an XY recorder. All detectors were calibrated in chopped effusive flows from the collimating chamber into the detection chamber. The detectors differ chiefly in that the ionizing electrons are accelerated relatively directly from the cathode to the anode in the Nier ionizer, are oscillated across the beam in the Heil ionizer, and are injected into an electrostatic field between two concentric cylinders with energies and angular momenta such that the electron paths are long in comparison with the radii of the cylinders in the orbitron detector. As a consequence of using the recurring pulsed beam, the ac amplifier, and the digital memory oscilloscope, beams with densities four orders of magnitude smaller than the background density have been detected.

### 3 BEAM DENSITY

For most operating conditions of the molecular beam described here, the translational degrees of freedom of the molecules in the free jet freeze upstream from the skimmer. For this case, Anderson and Fenn (Ref. [4]) suggest a model in which the flow near the centerline of the free jet is represented by spherically symmetric source flow and the freezing occurs suddenly at a value of the radius which depends upon the source conditions. In an application of this model to a relatively simple prediction of the number density of molecules at the detector, consider figure 2. If background scattering is negligible, then the differential flux per unit solid angle in the speed range between  $u$  and  $u+du$  emanating from a differential area of the sudden-freezing surface as seen at a point  $P$  on the beam axis may be written

$$dJ_{0d}(u, \xi, \alpha) = n_T u 2\pi x_T^2 \sin \xi \cos(\xi + \alpha) F(u, \xi, \alpha) u^2 du d\xi \quad (1)$$

where  $n_T$  is the number density at the sudden-freezing surface,  $2\pi x_T^2 \sin \xi d\xi \cos(\xi + \alpha)$  is the differential area on the spherical freezing surface as seen from point  $P$ ,  $F(u, \xi, \alpha)$  is the number of particles per unit volume of velocity space in the vicinity of the angle  $\xi + \alpha$  from the direction of the hydrodynamic velocity, and  $u^2 du$  is the differential volume in velocity space per unit solid angle. The distribution function is given by

$$F(u, \xi, \alpha) = [m/(2\pi kT)]^{3/2} \exp[-(\vec{s}_p - \vec{S}_T) \cdot (\vec{s}_p - \vec{S}_T)] \quad (2)$$

where  $m$  is the molecular mass,  $k$  is Boltzmann's constant,  $T$  is absolute temperature,  $s_p$  is the speed ratio of molecules with velocity in the direction of point  $P$ , and  $S_T$  is the hydrodynamic speed ratio at the sudden-freezing surface. The differential number density may be related to the differential flux per unit solid angle by

$$dn_{0d} = (dJ_{0d})/uL_{1d}^2 \quad (3)$$

where  $L_{1d}$  is the distance from the skimmer to the detector. Combining equations (1-3), one obtains

$$dn_{0d} = \frac{2x_T^2}{\pi^{3/2} L_{1d}^2} n_T s^2 \exp\{-[s^2 - 2sS_T \cos(\xi + \alpha) + S_T^2]\} \times \cos(\xi + \alpha) \sin \xi d\xi ds \quad (4)$$

For the case in which

$$x_T \ll L_{Td} \text{ [so that } \cos(\xi + \alpha) \approx \cos \xi]$$

and  $S_T \cos \xi_{\max} \gg 1$  [so that terms of order unity are negligible in comparison with  $(S_T \cos \xi_{\max})^2$ ], integration of equation (4) with respect to  $s$  and  $\xi$  yields

$$n_{0d} \approx n_T (x_T/L_{Td})^2 [1 - \exp(-S_T^2 \sin^2 \xi_{\max}) \cos^2 \xi_{\max}] \quad (5)$$

If beam attenuation due to background scattering is significant, then

$$n_d = n_{0d} \exp[-n_c \sigma_c L_{1d} - n_s \sigma_s (x_1 - x_{\max})] \quad (6)$$

where  $n_d$  is the number density at the detector,  $n_c$  is the background number density in the collimating chamber,  $\sigma_c$  is the effective cross section for scattering in the collimating chamber,  $n_s$  is the background number density in the source chamber,  $\sigma_s$  is the effective cross section for scattering in the source chamber, and  $x_1 - x_{\max}$  is the path length over which background scattering is important in the source chamber. In order to relate  $n_T$ ,  $x_T$ , and  $S_T$  to parameters which are measured more easily, use the isentropic relation for  $M_T \gg 1$

$$n_0/n_T = [1 + \frac{1}{2}(\gamma - 1) M_T^2]^{1/(\gamma - 1)} \approx [\frac{1}{2}(\gamma - 1) M_T^2]^{1/(\gamma - 1)} \quad (7)$$

the equation of state for a thermally perfect gas

$$n_0 = p_0/kT_0 \quad (8)$$

the equation for the mass-flow rate of a thermally perfect gas through a sonic throat

$$\dot{m} = \frac{p_0 m}{kT_0} \frac{\pi d^{*2}}{4} \left(\frac{\gamma k T_0}{m}\right)^{1/2} \left(\frac{2}{\gamma + 1}\right)^{(\gamma + 1)/2(\gamma - 1)} \quad (9)$$

the Mach number vs. distance relation of Ashkenas and Sherman (Ref. [5]) for  $\gamma = 5/3$  and  $x \gg d^*$

$$M_T = 3.31 (x_T/d^*)^{2/3} \quad (10)$$

the empirical relation of Anderson and Fenn (Ref. [4]) for the terminal Mach number

$$M_T = 1.17 (1/\text{Kn}_0)^{0.4} \quad (11)$$

and the approximate equations for  $\xi_{\max} \ll 1$

$$\sin \xi_{\max} \approx d_1/2 x_T \quad (12)$$

$$\cos \xi_{\max} \approx 1 \quad (13)$$

where  $n_0$  is the number density in the stagnation chamber,  $M_T [\equiv (2/\gamma)^{1/2} S_T]$  is the Mach number at the sudden-freezing surface,  $p_0$  is the pressure in the stagnation chamber,  $T_0$  is the absolute temperature in the stagnation chamber,  $\dot{m}$  is the mass-flow rate through the source orifice,  $d^*$  is the diameter of the source orifice,  $\text{Kn}_0 [\equiv \lambda_0/d^*]$  is the Knudsen number based on source conditions,  $\lambda_0 [\equiv 1/(2)^{1/2} n_0 \sigma_0]$  is the mean-free-path length in the source chamber, and  $\sigma_0$  is the cross section for collisions in the source chamber. If one eliminates  $n_{0d}$ ,  $n_T$ ,  $T_0$ ,  $x_T$ ,  $M_T$  (hence also  $S_T$ ),  $\sin \xi_{\max}$ , and  $\cos \xi_{\max}$  from equations (5-13), one may write finally for  $\gamma = 5/3$

$$\ln \left[ \frac{2.27 n_d m p_0 d^{*2} L_{Td}^2 / \dot{m}^2}{1 - \exp[-6.45 \text{Kn}_0^{0.4} (d_1/d^*)^2]} \right] \approx -n_c \sigma_c L_{12} - n_s \sigma_s (x_1 - x_{\max}) \quad (14)$$

For fixed values of pumping speeds, skimmer-collimator distance, and stagnation temperature, the convenient independent parameters in equation (14) are source-orifice diameter  $d^*$ , skimmer orifice diameter  $d_1$ , source-skimmer distance  $x_1$ , and source mass flow  $\dot{m}$ . This equation will be used both to correlate

measured values of the beam density and to maximize the beam density. Keep in mind that in such applications this equation must be supplemented by criteria for formation of a free-jet shock-structure and for interaction of the free jet with the skimmer.

For the earlier beam-density measurements, the two-disc turbine-driven chopper-filter (with a reduced phase angle of about  $4^\circ$ ) was placed in the detection chamber, and a Nier-ionizer detector was mounted approximately 10 cm downstream from the second disc. Under these conditions, if the chopper-filter is rotated at a speed such that the most-probable transmitted speed is near the most-probable beam speed, then the transmission [Ref. [1], Equ. (28)] is close to unity and the time-of-flight resolution [Ref. [1], Equ. (46)] is significantly greater than unity so that the peak chopped-beam density at the detector differs negligibly from the unchopped-beam density at the same skimmer-detector distance (approximately 180 cm). The beam density was measured for  $d_1/d^*$  ratios from 9 to 115, stagnation-chamber Knudsen numbers from 0.0018 to 0.0059, stagnation temperatures from 2800 to 4300°K, source-chamber pressures from  $4 \times 10^{-3}$  to  $2 \times 10^{-2}$  Torr and collimating-chamber pressures from  $2 \times 10^{-5}$  to  $2 \times 10^{-4}$  Torr. The higher source-chamber and collimating-chamber pressures were produced by admitting argon via a needle valve to the appropriate chamber.

Values of the beam density measured in these experiments are plotted as functions of dimensionless nozzle-skimmer distance, collimating-chamber pressure, and source-chamber pressure in figures 3-5. Figure 3 illustrates the attenuation of the beam at low  $x_1/d^*$  ratios due to collimating-chamber background scattering and skimmer interference and at high  $x_1/d^*$  ratios due to source-chamber background scattering. The slope of the line drawn in figure 4 corresponds to an effective cross section of about

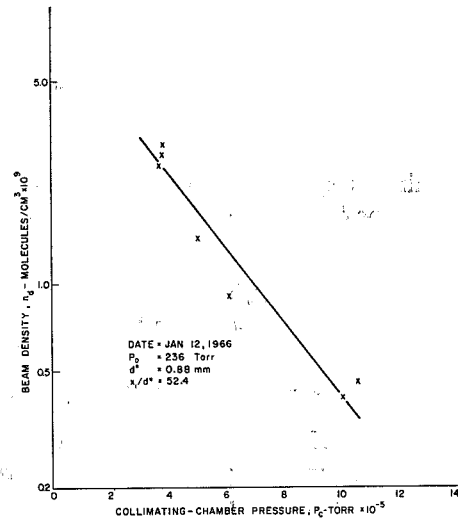


Fig. 4 Beam Attenuation due to Background Scattering in the Collimating Chamber

$90 \cdot A^2$  for collimating chamber background scattering. [See Equ. (6).] If one uses in equation (6) the values of  $x_{\max}$  predicted by the equation written by Brown and Heald (Ref. [6]) on the basis of the measurements by Fenn and Anderson (Ref. [7]), then the lines drawn in figure 5 correspond to an effective cross section of

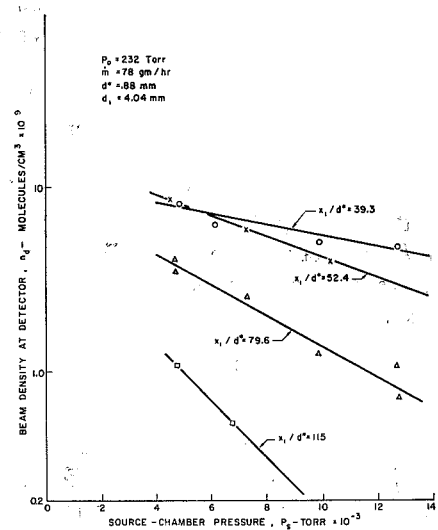


Fig. 5 Beam Attenuation due to Background Scattering in the Source Chamber (Beam density has been corrected to zero pressure in the collimating chamber)

about  $11.5 A^2$  for source-chamber background scattering. These values of the effective cross sections are used in figure 6 in an attempt to correlate all of the earlier beam-density measurements by use of the coordinates suggested by equation (14).

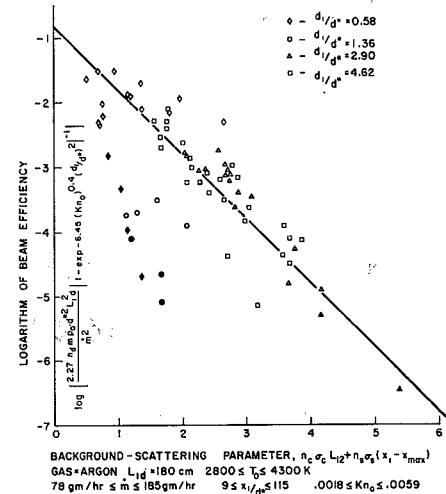


Fig. 6 Beam Efficiency as a Function of Background Scattering

Inspection of figure 6 reveals that, at least for the parameter ranges represented in this figure, the coordinates suggested by equation (14) are useful in correlations of measured densities of supersonic

atomic beams. (Only slight modifications would be required to adapt the derivation presented here to supersonic beams of more complicated molecules.) The large deviations of the filled symbols from the correlating line are due perhaps to skimmer interference. (For all of these points,  $x_1 < x_{\max}$ .) The deviations of the circles from the correlating line are due perhaps to the gross imperfections discerned in the leading edge of the skimmer used in the experiments associated with these points. The fact that the effective cross section for source-chamber background scattering is much smaller than the effective cross section for collimating-chamber scattering is explained (at least in part) by the fact that the angular resolution for scattering is much smaller in the collimating chamber than in the source chamber. Since the coordinates used in figure 6 are based upon a more complete model of beam generation than used in reference [1], these coordinates supercede the coordinates used in figure 15 of reference [1]. The weakest step in this correlation is perhaps the prediction of the path length  $x_1 - x_{\max}$  over which background scattering is important in the source chamber.

For the later beam-density measurements, the motor-driven chopper was placed in the collimating chamber, and an orbitron detector was mounted approximately 65 cm downstream from the chopper disc. The beam density was measured for  $d_1/d^* = 0.80$ ,  $x_1/d^*$  ratios from 13 to 25, stagnation-chamber Knudsen numbers from 0.0045 to 0.023, a stagnation temperature of 9000°K, source-chamber pressures from  $2 \times 10^{-3}$  to  $3 \times 10^{-1}$  Torr, and collimating-chamber pressures from  $1 \times 10^{-5}$  to  $4 \times 10^{-5}$  Torr. Since the chopper can not be run at speeds sufficiently slow so that the time-of-flight resolution is large in comparison with unity, the unchopped-beam density was calculated using equation (28) of the following section. In order to facilitate comparisons with the earlier beam-density measurements, the later measure-

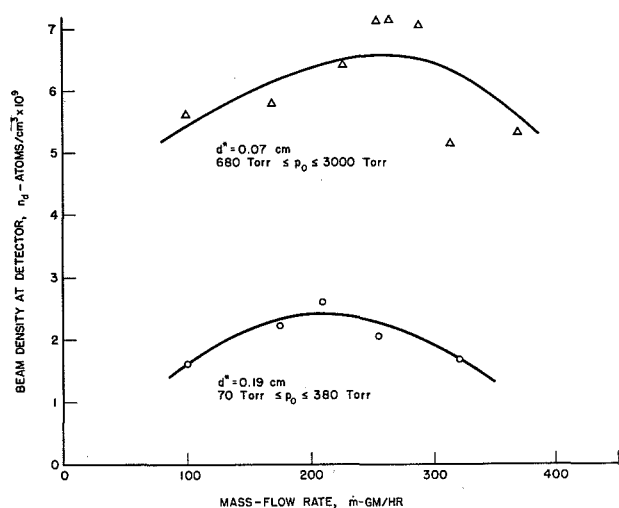


Fig. 7 Beam Density vs. Source-Orifice Mass-Flow Rate (Beam energy = 1.9 eV,  $d_1 = 0.152$  cm,  $L_{1d} = 180$  cm, nozzle-skimmer distances optimized)

ments were adjusted to a skimmer-detector distance of 180 cm.

Values of the beam density measured in these experiments are plotted as a function of nozzle mass-flow rate in figure 7. This figure illustrates the attenuation of the beam at high nozzle mass-flow rates due to background scattering and skimmer interference. An attempt to correlate these data using the procedure of figure 6 reveals that this procedure is inadequate for the parameter ranges investigated here. The chief difference in the parameter ranges was that the Knudsen numbers in the later experiments were significantly greater than in the earlier experiments. Since the Knudsen number has a greater effect on  $x_1 - x_{\max}$  than on any other parameter appearing in the coordinates of figure 6, the equation used in the prediction of  $x_{\max}$  was examined. Values of  $x_{\max}$  required to place these data on a line (with a slope corresponding to the forementioned values of the effective cross sections and with an intercept, about -1.2, determined by extrapolation to zero background densities) are presented in figure 8 and compared with the correlation line of Fenn and Anderson (Ref. [7]) and with the data of Brown and Heald (Ref. [6]). Beam intensities up to  $7 \times 10^{19}$  atoms/steradian-sec were observed during these experiments.

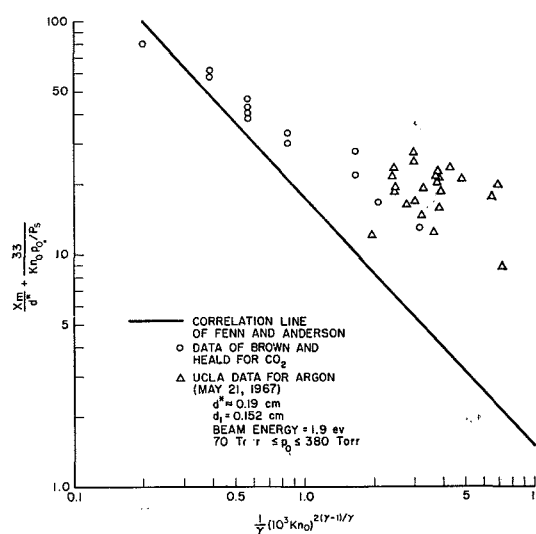


Fig. 8 Correlation of Source-Chamber Scattering Conditions

Inspection of figure 8 indicates that the values of  $x_{\max}$  reported here agree better with the data of Brown and Heald than with the correlation line of Fenn and Anderson. The difference between the values reported here and the line of Fenn and Anderson may be due in part to a difference in definition. Fenn and Anderson define  $x_{\max}$  as the nozzle-skimmer distance at which the detector signal is a maximum whereas  $x_{\max}$  is defined here as the nozzle-skimmer distance required to provide a correlation of the type shown in figure 6, a correlation which does not assume that the beam intensity is a maximum at  $x_1 = x_{\max}$ . Since the intercepts for the correlations of the data taken with the chopper-filter and with the chopper are

approximately equal, it is concluded that the second disc of the chopper-filter reduced negligibly the peak chopped-beam density measured at the detector. The realized beam intensities (expressed in atoms/steradian-sec) are about the same as observed for other supersonic molecular beams.

For operating conditions under which equation (14) is applicable (translational freezing upstream from the skimmer and negligible effects of free jet shock structure and skimmer interactions), this equation may be used as a guide in the search for the operating conditions which maximize the beam density. Consider the case in which the source-chamber pumping speed, collimating-chamber pumping speed, stagnation temperature, skimmer-collimator distance, and source-orifice diameter are fixed by other considerations. Then a convenient choice of the three remaining independent system parameters is the skimmer-orifice diameter  $d_1$ , the source-skimmer distance  $x_1$ , and the source-orifice mass flow  $\dot{m}$ . Conditions for maximum beam density are obtained by solving equation (14) for the number density  $n_d$  and setting its derivatives with respect to the three independent system parameters equal to zero. In the differentiations performed here, the scattering length in the source chamber and the number density in the collimating chamber were predicted respectively by the equation of Brown and Heald (with one term neglected):

$$(x_1 - x_{\max})/d^* \approx x_1/d^* - 0.085/\text{Kn}_0^{0.86} \quad (15)$$

and by the steady-state flow equation (with source-chamber background-gas effusion neglected)

$$n_c S_c \approx n_T (x_T/x_1)^2 \pi/4 d_1^2 U_T \quad (16)$$

where  $S_c$  is the collimating-chamber pumping speed and  $U_T$  is the hydrodynamic speed at the sudden-freezing surface. Setting the derivatives of  $n_d$  with respect to  $d_1$ ,  $x_1$ , and  $\dot{m}$  equal to zero, one obtains respectively the three equations

$$n_c S_c L_{12} = \frac{6.45 \text{Kn}_0^{0.4} (d_1/d^*)^2}{\exp [6.45 \text{Kn}_0^{0.4} (d_1/d^*)^2] - 1} \quad (17)$$

$$n_c S_c L_{12} = \frac{1}{2} (n_s \sigma_s x_1) \quad (18)$$

$$n_c S_c L_{12} = [1 - n_s \sigma_s (x_1 - 1.86 x_{\max})]/1.4 \quad (19)$$

If the value of  $\dot{m}$  predicted by these equations exceeds the capability of the source-chamber pumping system, then  $\dot{m}$  is fixed by the characteristics of this pumping system and equation (19) is omitted. If the value of  $x_1$  predicted by these equations is less than  $x_{\max}$ , then  $x_1$  is equated to  $x_{\max}$  and equation (18) is omitted. Calculations were made for several source-orifice

diameters and the special case in which  $\sigma_c = 90 \text{ \AA}^2$ ,  $L_{12} = 100 \text{ cm}$ ,  $T_0 = 5700 \text{ }^\circ\text{K}$ ,  $S_c = 4000 \text{ liters/sec}$ , and the maximum throughput of the source-chamber pumping system is  $250 \text{ g/h}$ . For this special case,  $\dot{m}$  and  $x_1$  are limited respectively by the maximum throughput of the source-chamber pumping system and by skimmer interference so that only equation (17) needs to be solved. Limiting values of  $\dot{m}$  and  $x_1$ , predicted optimum values of  $d_1$ , and resulting values of  $p_0$ ,  $M_T$ , and  $n_d$  are given in figure 9 as a function of source-orifice diameter. Since both the beam density and the terminal Mach number increase as the source-orifice diameter decreases, their maximum values are

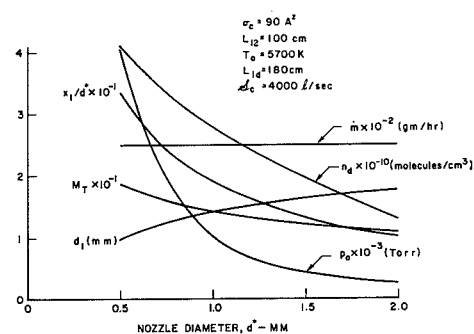


Fig. 9 Maximized Beam Density and Corresponding System Parameters as Function of Nozzle Diameter

limited by the minimum feasible value of the source-orifice diameter. This analysis motivated several changes in the facility (including the addition of another diffusion pump to the collimating chamber and the doubling of the heater output in the diffusion pump for the source chamber) which quadrupled the beam intensity to its present value of about  $7 \times 10^{19}$  atoms/steradian-sec.

#### 4 BEAM SPEED DISTRIBUTION

The beam speed distribution was measured using the time-of-flight technique. In order to obtain relatively simple procedures for determining the hydrodynamic speed ratio  $S_T$  and the unchopped-beam density from measured time-of-arrival distributions, consider the time-of-arrival distribution which follows from equation (4). Represent the time of departure at the chopper by  $t_f$  and the time of arrival at the detector by  $t_d$  so that

$$u = L_{fd}/(t_d - t_f), \quad (20)$$

where  $L_{fd}$  is the distance from the chopper to the detector. Then, for the case in which  $x_T \ll L_{Td}$  [so that  $\cos(\xi + \alpha) \approx \cos \xi$ ], equation (4) may be written

$$dn_d(t_d, t_f, \xi) = \frac{n_T L_{fd}^3}{L_{1d}^2} 2\pi x_T^2 \left( \frac{m}{2\pi k T_T} \right)^{\frac{3}{2}} \exp \left\{ -\frac{m}{2k T_T} \left[ \left( \frac{L_{fd}}{t_d - t_f} \right)^2 - \frac{2 L_{fd} U_T \cos \xi}{t_d - t_f} + U_T^2 \right] \right\} \frac{\cos \xi \sin \xi f_f(t_f)}{(t_d - t_f)^4} d\xi dt_f \quad (21)$$

where  $f_f(t_f)$  is the chopper shutter function (with value between 0 and 1). Integration of equation (21) by parts with respect to  $\xi$  and omission of terms of first and higher orders in  $1/S_T$  yields

$$ln_d(t_d, t_f) \approx \frac{n_T L_{fd}^2}{L_{1d}^2} \frac{x_T^2}{U_T} \left( \frac{m}{2\pi k T_T} \right)^{\frac{1}{2}} \frac{1}{(t_d - t_f)^3} \left\langle \exp \left\{ -\frac{m}{2k T_T} \left[ \frac{L_{fd}}{t_d - t_f} - U_T \right]^2 \right\} - \exp \left\{ -\frac{m}{2k T_T} \left[ (U_T \sin \xi_{\max})^2 + \left( \frac{L_{fd}}{t_d - t_f} - U_T \cos \xi_{\max} \right)^2 \right] \right\} \cos \xi_{\max} \right\rangle f_f(t_f) dt_f \quad (22)$$

By appropriate operations on this distribution function, expressions for both the (easily measured) maximum value of and total area under the time-of-arrival distributions are obtained. These two expressions may be solved simultaneously for  $U_T$  and  $T_T$  (and, hence,  $S_T$ ). For definiteness, consider now the simplified (but interesting) case in which the time-of-flight resolution is small (i.e., all molecules in one burst may be considered to leave the chopper simultaneously) and  $\exp[-2 S_T^2(1 - \cos \xi_{\max})] \ll 1$ . Then equation (22) simplifies to

$$n_d(t_d) \approx n_T \left( \frac{x_T}{L_{1d}} \right)^2 \frac{L_{fd}^2}{U_T t_d^3} \left( \frac{m}{2\pi k T_T} \right)^{\frac{1}{2}} \exp \left\{ -\frac{m}{2k T_T} \left[ \frac{L_{fd}}{t_d} - U_T \right]^2 \right\} \int f_f(t_f) dt_f \quad (23)$$

where the indicated integration is over the entire range of departure times for a given burst. If  $S_T \gg 1$ , then the maximum value of the number density occurs at

$$L_{fd}/t_d \approx U_T. \quad (24)$$

and is given by

$$n_d(t_d)_{\max} \approx n_T \left( \frac{x_T}{L_{1d}} \right)^2 \frac{S_T}{\pi^{\frac{1}{2}}} \frac{U_T}{L_{fd}} \int f_f(t_f) dt_f \quad (25)$$

The total area under the time-of-arrival distribution is

$$\int_0^\infty n_d(t_d) dt_d \approx n_T \left( \frac{x_T}{L_{1d}} \right)^2 \int f_f(t_f) dt_f \quad (26)$$

In principle, equations (25-26) could be solved simultaneously for  $U_T$  and  $T_T$ . In practice, since  $U_T$  can be determined relatively easily from the time-of-flight distribution when  $S_T \gg 1$ , it is more convenient to eliminate the integral from the right-hand sides of equations (25-26) to obtain

$$S_T \approx \pi^{\frac{1}{2}} \frac{L_{fd}}{U_T} \frac{n_d(t_d)_{\max}}{\int_0^\infty n_d(t_d) dt_d} \quad (27)$$

Eliminating  $n_T(x_T/L_{1d})^2$  from equations (5) and (26), one finds that, for the case in which

$$\exp[-2 S_T^2(1 - \cos \xi_{\max})] \approx \exp[-S_T^2 \sin^2 \xi_{\max}] \ll 1,$$

the unchopped-beam density is related to the area under the time-of-flight distribution by

$$n_{d, \text{unchopped beam}} \approx \frac{\int_0^\infty n_d(t_d) dt_d}{\int f_f(t_f) dt_f} \quad (28)$$

Equation (23), with  $U_T$  and  $T$  obtained from equations (24) and (27) and the definition of  $S_T$ , will be compared with measured time-of-flight distributions; equation (28) was used in computations of unchopped-beam density from chopped-beam measurements.

The speed distributions were measured with the chopper mounted in the collimating chamber and the Heil-ionizer detector mounted about two meters downstream on the beam axis. Time-of-arrival distributions

were monitored at a time-of-flight resolution [Ref. [1], Equ. (46)] of 0.26,  $d_1/d^*$  ratios from 2.0 to 7.0,  $x_1/d^*$  ratios from 39 to 110, and nozzle stagnation Knudsen numbers from  $2.6 \times 10^{-3}$  to  $1.4 \times 10^{-2}$ . The light emanating from the arc jet (and passing through the chopper slot) provided the zero-time reference signal whereas the output of a light and photocell, mounted on the chopper base on opposite sides of the disc, provided a signal for triggering the oscilloscope sweep and monitoring the chopper speed.

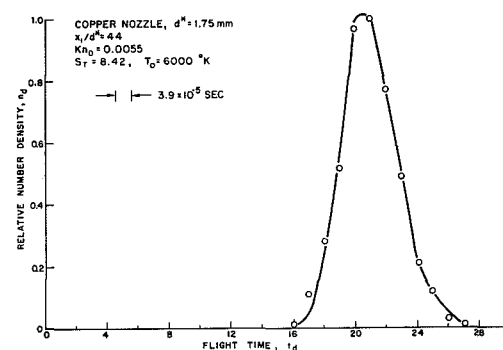


Fig. 10 Comparison of Predicted and Measured Flight-Time Distributions

A typical measured time-of-flight distribution is shown in figure 10. Each data point represents the reading from one channel of the digital memory oscilloscope. Since these distributions were measured at values of  $x_1/d^*$  sufficiently large that the measured Mach numbers were terminal values, they are plotted as a function of  $\text{Kn}^{-0.4}$  in figure 11. The collision cross sections used in the computation of  $\text{Kn}_0$  were based on a modified Buckingham (exp-6) potential and the beam kinetic temperature computed from time-of-flight measurements. The data for the 1.75-mm copper nozzle are seen to agree better with the empirical curve of Anderson and Fenn (Ref. 4) than do the data for the 0.58-mm tungsten nozzle. The beam kinetic temperature is compared with the stagnation temperature, computed from equation (9), in figure 12 for the two different nozzles. The two temperatures are nearly equal for the 1.75-mm copper nozzle whereas the beam kinetic temperature is about 1.6 times the stagnation temperature for the 0.58-mm tungsten



nozzle. Realized beam energies are presently of the order of 2 eV. Kessler and Koglin (Ref. 8) showed that adding an insulated intermediate electrode can increase the beam energy to nearly 6 eV.

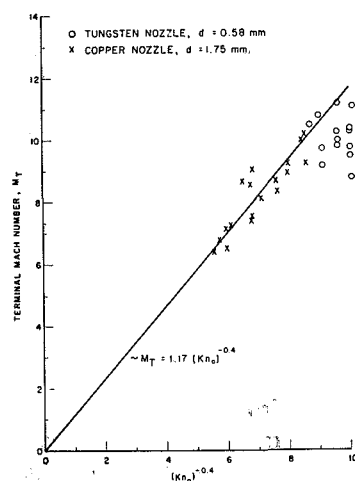


Fig. 11 Terminal Mach Number vs.  $Kn^{-0.4}$

For the conditions under which the time-of-arrival distributions were measured, the value of  $\exp[-2 S_T^2(1 - \cos \xi_{\max})]$  was found to be small in comparison with unity. Hence the measured distribution is compared, in figure 10, with the distribution predicted by equation (23) for values of  $U_T$  and  $T_T$

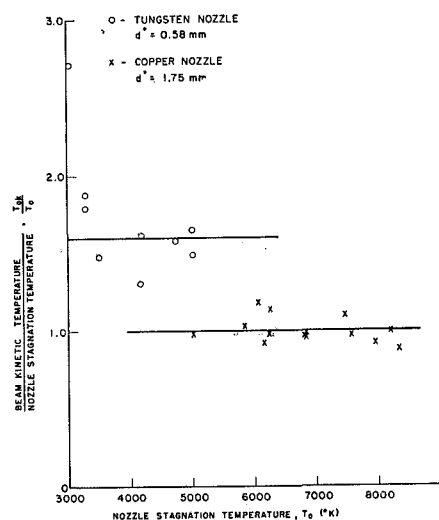


Fig. 12 Ratio of Beam Kinetic Temperature to Nozzle Stagnation Temperature as a Function of Nozzle Stagnation Temperature

obtained using equations (24) and (27) and the definition of  $S_T$ . The measured and predicted values agree within the probable experimental error. Errors due to uncertainties in the departure time of molecules from the chopper and the finite time resolution of the digital memory oscilloscope are estimated to be less than 2 percent. A measure of the errors due to background scattering is provided by the prediction that, if  $1/e$  of the molecules are scattered at a mean beam speed of 2500 m/sec and the scattering cross section varies as

$u^{-1/5}$ , than 8 percent more molecules with speeds of 2000 m/sec are scattered out of the beam than molecules with speeds of 3000 m/sec. The origin of the difference in the performance of the 0.58-mm tungsten nozzle and the 1.75-mm copper nozzle indicated in figures 11 and 12 is not apparent at this time.

## 5 BEAM IONIZATION AND EXCITATION

In order to interpret the data acquired in applications of this facility (e.g., in studies of atom-atom collisions and atom-surface collisions), information concerning the states of the beam particles is required. Hence the forementioned measurements of beam density and speed distribution were supplemented by measurements (made with the aid of an Auger detector) of the flux of ions and excited particles (Ref. [9]).

For a 1.52 eV argon beam extracted from a source at a stagnation pressure of 178 Torr and with an orifice diameter of 2 mm, it was found that (a) the speed of the excited-state neutral particles is 6 percent less than the speed of the ground-state neutral particles, (b) the fractional ionization is about  $1.16 \times 10^{-6}$ , and (c) the fractional excitation is about  $3.86 \times 10^{-4}$ . It was concluded that (a) the ions are molecular during at least a portion of the free jet expansion, (b) nearly all of the ions are neutralized during this expansion, and (c) most of the excited particles formed as a consequence of this neutralization are long-lived.

The measured fractions are believed to have negligible effects on all present applications of this facility. However, they would have to be taken into account in those special particle-particle collision studies in which cross sections for collisions with either ionized or excited beam particles are orders of magnitude greater than collisions with ground-state neutral beam atoms.

## 6 APPLICATIONS

Although the primary purpose of this paper is to review recent studies of the density and speed distribution in the arc-heated supersonic molecular beam, a brief summary of applications of this facility is included here. These applications included studies of both atom-surface and atom-atom collisions.

In the earlier studies of atom-surface collisions, the scattering of a 1-eV argon beam from several surfaces with varying degrees of contamination was monitored for fixed conditions of the chopped incident beam but for several values of the scattering angle. The reported measurements (References 3 and 10) were limited to an incidence angle of  $60^\circ$  from the surface normal and mostly to scattering angles in the plane defined by the incident beam and the surface normal (the  $\phi = 0$  plane). The scattering distributions in the forementioned plane were found, unexpectedly, to consist of multiple lobes (Figs. 6 through 9 of Ref. [3]) — even for polycrystalline and/or contaminated surfaces for which completely diffuse scattering of thermal-energy beams would be expected. Within the accuracy

of the presented data, and for the range of conditions investigated, three lobes were observed. Some of the results of subsequent extensions of the earlier studies

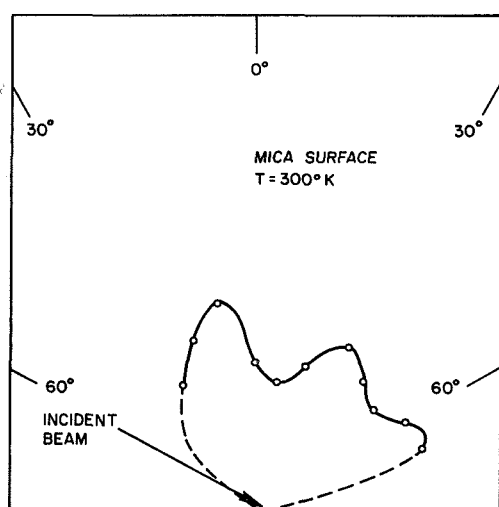


Fig. 13 Scattering Distribution for 1 eV Argon Beam Impinging on Contaminated Room-Temperature Mica Surface (Incidence angle = 60° from surface normal;  $\phi = 0^\circ, 180^\circ$ .) From figure 5.4 of reference [10]

are presented in figures 13 and 14, where scattering distributions for 1-eV argon beams impinging on contaminated room-temperature mica surfaces are given. It was found that (a) as the incidence angle is reduced from 60° to 50°, the two forward-scattering lobes appear to shift toward the surface normal (not shown here), (b) as the incidence angle is increased from 60° to 70°, the two forward-scattering lobes appear to shift away from the surface normal, the back-scattering lobe appears to shift into the forward-scattering region, and another lobe appears in the back-scattering region (fig. 13 and 14) and (c) the scattering (including the scattering in the back-scattering lobe) is concentrated near the  $\phi = 0$  plane (not shown here). Efforts are concentrated presently on measuring the masses and speeds of the scattered particles.

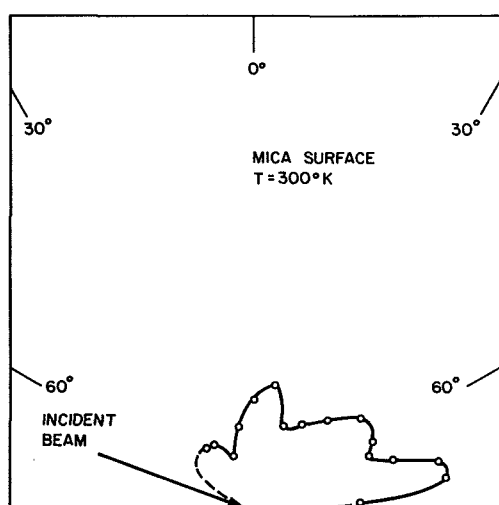


Fig. 14 Scattering Distribution for 1 eV Argon Beam Impinging on Contaminated Room-Temperature Mica Surface (Incidence angle = 70° from surface normal;  $\phi = 0^\circ, 180^\circ$ )

Integral cross sections for elastic argon-argon collisions at one electron volt have been measured in preliminary studies of atom-atom collisions (Refs. [1] and [2]). The scattering gas was contained in a chamber 21.5 cm in length which was attached in the collimating chamber to the wall separating the collimating chamber from the detection chamber. The incident beam was speed filtered by the two-disc motor-driven chopper-filter; the transmitted beam was detected by a Heil-ionizer detector. Measurements made with an angular resolution of 2.2° were extrapolated analytically to obtain an integral cross section of 273 Å<sup>2</sup> for argon-argon scattering at 2360 m/sec. This value compares favorably with 266 Å<sup>2</sup> at 2360 m/sec extrapolated from the thermal-energy data of Rothe *et al.* (Ref. [11]). Future studies will include measurements, using a supersonic atomic beam and a cooled scattering gas, of integral cross sections for elastic dissimilar-atom collisions as a function of collision energy.

## 7 ACKNOWLEDGMENT

Wayne E. Rodgers contributed significantly to the recent beam density measurements described here.

## REFERENCES

- [1] KNUTH, E.L. and KULUVA, N.M., "Performance of an Arc-Heated Supersonic Molecular Beam and its Application to Molecule-Molecule Collision Studies," *Recent Advances in Aerothermochemistry*, I. Glassman, ed., vol. 1, pp. 277-338. NATO Advisory Group for Aerospace Research and Development, Paris, 1967.
- [2] KULUVA, N.M., "Performance of an Arc-Heated Supersonic Molecular Beam and its Application to Molecule-Molecule Collision Studies," *Report No. 67-11*. Department of Engineering, University of California, Los Angeles, April 1967.
- [3] ALCALAY, J.A. and KNUTH, E.L., "Experimental Study of Scattering in Particle-Surface Collisions with Particle Energies of the Order of 1 eV," *Rarefied Gas Dynamics* (C.L. Brundin, ed.), vol. I, pp. 253-268. Academic Press, New York, 1967.
- [4] ANDERSON, J.B. and FENN, J.B., "Velocity Distributions in Molecular Beams from Nozzle Sources," *Physics of Fluids* 8:780-787, May 1965.
- [5] ASHKENAS, H. and SHERMAN, F.S., "The Structure and Utilization of Supersonic Free Jets in Low Density Wind Tunnels," *Rarefied Gas Dynamics* (J.H. de Leeuw, ed.), vol. II, pp. 84-105. Academic Press New York, 1966.
- [6] BROWN, R.F. and HEALD, J.H., Jr., "Background Gas Scattering and Skimmer Interaction Studies Using a Cryogenically Pumped Molecular Beam Generator," *Rarefied Gas Dynamics* (C.L. Brundin, ed.), vol. III, pp. 1407-1426. Academic Press, New York, 1967.
- [7] FENN, J.B., and ANDERSON, J.B., "Background and Sampling Effects in Free Jet Studies by Molecular Beam Measurements," *Rarefied Gas Dynamics* (J.H. de Leeuw, ed.), vol. II, pp. 311-330. Academic Press, New York, 1966.
- [8] KESSLER, R.W. and KOGLIN, B., "Production of Fast Molecular Beams Using Supersonic Plasma Jet," *Rev. Sci. Instr.* 37:682, May 1966.
- [9] WINICUR, D.H. and KNUTH, E.L., "Measurement of Excitation and Ionization in an Arc-Heated Supersonic Argon Beam," *J. Chem. Phys.* 46:4318-4320, June 1967.
- [10] ALCALAY, J.A., "Experimental Study of Scattering in Atom-Surface Collisions with Atom Energies of the Order of 1 eV," *Report No. 67-20*. Department of Engineering, University of California, Los Angeles, May 1967.
- [11] ROTHE, E.W., MARINO, L.L., NEYNABER, R.H., ROL, P.K. and TRUJILLO, S.M., "Scattering of Thermal Rare Gas Beams by Argon. Influence of the Long-Range Dispersion Forces," *Physical Review* 126:589-602, April 1962.